

As vacancies, Ga antisites, and Au impurities in zinc blende and wurtzite GaAs nanowire segments from first principles

Yaojun A. Du,^{*} Sung Sakong, and Peter Kratzer

Fakultät für Physik and Center for Nanointegration (CENIDE), Lotharstraße 1, 47048 Duisburg, Germany

(Received 21 August 2012; revised manuscript received 8 November 2012; published 8 February 2013)

In this paper some specific issues related to point defects in GaAs nanowires are addressed with the help of density functional theory calculations. These issues mainly arise from the growth of nanowires under conditions different from those used for thin film or bulk GaAs, such as the coexistence of zinc blende and wurtzite polytypes, the use of gold particles as catalyst, and the arsenic-limited growth regime. Hence, we carry out density functional calculations for As vacancies, Ga_{As} antisites, and Au impurities in zinc blende (ZB) and wurtzite (WZ) GaAs crystals. Our results show that As vacancies can diffuse within a ZB GaAs crystal with migration barriers of ~ 1.9 eV. Within WZ GaAs, As vacancy diffusion is found to be anisotropic, with low barriers of 1.60 up to 1.79 eV (depending on doping conditions) in the *ab* plane, while there are higher barriers of 2.07 to 2.44 eV to diffuse along the *c* axis. The formation energy of Au impurities is found to be generally much lower than those of arsenic vacancies or Ga_{As} antisites. Thus, Au impurities will be the dominant defects formed in Au-catalyzed nanowire growth. Moreover, we find that it is energetically more favorable by 1 to 2 eV for a Au impurity to replace a lattice Ga atom than a lattice As atom in GaAs. A Au substitutional defect for a lattice Ga atom in ZB GaAs is found to create a charge transfer level in the lower half of the band gap. While our calculations locate this level at $E_v + 0.22$ eV, taking into account the inaccuracy of the density functional that ought to be corrected by a downshift of E_v by about 0.2 eV, results in good agreement with the experimental result of $E_v + 0.4$ eV.

DOI: [10.1103/PhysRevB.87.075308](https://doi.org/10.1103/PhysRevB.87.075308)

PACS number(s): 73.22.-f, 71.55.Eq, 81.07.Gf, 66.30.Lw

I. INTRODUCTION

Semiconductor nanowires have been emerging as a promising building block for various nanodevices.¹ These potential applications include light emitters,² solar cells,³ and microelectronics.^{4,5} All these applications require that it be possible to keep the concentration of intrinsic defects and impurities in the nanowires below a given threshold so as to enable long exciton lifetimes and to avoid unintentional doping due to electrically active impurities. In recent years, much experimental effort^{6–10} has been devoted to the fast and controllable growth of nanowires that is desired for reliable devices; and a gold nanoparticle is often used as a catalyst to promote the growth of GaAs nanowires. However, a Au droplet that accelerates a nanowire growing underneath can also leave impurities within the GaAs nanowire.^{11,12} Previous experimental efforts have focused on characterizing Au defect levels within a GaAs crystal.^{13–15} Moreover, experimental studies employing x-ray energy-dispersive spectroscopy^{7,11} indicate deviations from stoichiometry in the nanowires close to the growth zone, and thus point to the abundant intrinsic defects, in addition to Au impurities, in GaAs nanowires. While carrier lifetimes in core-shell nanowires from Au-free self-catalyzed growth^{16,17} were found to be much longer than in nanowires from Au-catalyzed growth,¹² they still fall short of the values reported for bulk samples by several orders of magnitude. This may indicate a higher level of growth-related intrinsic defects (as compared to the bulk) even in Au-free nanowires.

The focus of our interest is the defects that could be formed in nanowire growth below a metal nanoparticle. While the most abundant defect in low-temperature-grown bulk GaAs is the As antisite,¹⁸ we expect this defect *not* to play a role under the more Ga-rich growth conditions beneath a metal catalyst

particle. It is known that near the melting point and under the conditions typical of liquid-phase epitaxy, As vacancies are the dominant defects in GaAs.¹⁹ Furthermore, under As-deficient conditions, the As lattice site might remain unoccupied (As vacancy V_{As}), it could be occupied by gallium (Ga antisite Ga_{As}), or, in the case of growth with a gold catalyst, it may be occupied by a Au atom (Au_{As}). Since there is a general interest in possibly detrimental effects of Au on the properties of GaAs nanowires, we include Au_{Ga} defects in our study.

In this context, one has to consider that the effective growth conditions for the nanowire material are probably very different from the moderately arsenic-rich conditions commonly used in GaAs thin film growth. This is for the following reasons: In nanowire growth, material deposited from the vapor phase onto the substrate, the sidewalls, and the metal nanoparticle can reach the interfacial area between the nanowire tip and the particle via surface diffusion^{6,20–22} or diffusion through the liquid metal particle.²³ It is clear that sufficient Ga atoms can reach the interfacial growth zone at the nanowire tip, since the catalyst particle actually consists of a Au-Ga alloy.⁸ The situation is less clear concerning the As supply, since the low-pressure solubility of As in gold is low (in Au-catalyzed growth), and a high temperature leads to As loss (in self-catalyzed growth). In these cases, one would expect As-deficient growth conditions at the nanowire-particle interface. One possible scenario is that additional arsenic can reach the growth zone via an As vacancy diffusion mechanism through the GaAs nanowire. Moreover, under As-deficient conditions, one would also expect that As vacancies could be left behind within the GaAs nanowire by the advancing interfacial growth zone. A subsequent annealing process in arsenic vapor might be helpful to remove these vacancies. Therefore, it is important to understand V_{As} diffusion within GaAs bulk,

in order to comprehensively understand the As supply path during the growth process and to estimate a suitable annealing temperature for removing V_{As} s in a nanowire. A previous theoretical study based on density functional theory^{24,25} (DFT) calculated relatively high migration barriers of ~ 2.4 eV for a V_{As} in zinc blende GaAs.²⁶ This seemingly implies that As transport through the nanowire could be inefficient. However, the convergence of the atomic-orbital basis sets employed in these DFT calculations has not been demonstrated.

While wurtzite GaAs cannot be obtained in bulk form by ordinary growth techniques, GaAs nanowires grown with a Au catalyst may exhibit both zinc blende (ZB) and wurtzite (WZ) structures, or alternating segments of these (and other) polytypes through stacking faults.^{7,27–29} Hence, it is crucial to understand V_{As} , Ga_{As} , and Au impurities in *both* ZB and WZ GaAs crystals. There is considerable knowledge, from both the experimental¹⁹ and theoretical^{30,31} sides, about intrinsic point defects in ZB GaAs. However, experimental data on point defects in WZ GaAs are still elusive. In this work, we perform plane-wave DFT calculations to study various properties associated with V_{As} , Ga_{As} , and Au defects in ZB and WZ GaAs crystals, and to investigate and compare V_{As} diffusion in the two GaAs polytypes. This paper is organized as follows: The computational approach and supercell models are described in Sec. II. The formation energies of V_{As} and Ga_{As} defects and Au impurities in ZB and WZ GaAs crystals are discussed in Sec. III. The diffusion of V_{As} in various charge states in ZB and WZ GaAs crystals is presented in Sec. IV. We summarize our work in Sec. V.

II. METHODS OF CALCULATION

In this work, we have performed DFT calculations to study V_{As} , Ga_{As} , and substitutional Au impurities in ZB and WZ GaAs using the supercell method. The conventional unit cells for a ZB and a WZ GaAs crystal are shown in Fig. 1. Sufficiently large supercells of 216 (ZB) or 96 (WZ) atoms are used to fully relax the strain induced by defects and impurities. We employ the projector augmented-wave (PAW) method^{32,33} as implemented in the VASP code^{34,35} for all DFT calculations. The PAW potentials include $4s4p$, $4s4p$, and $5d6s$ electrons as valence electrons for As, Ga, and Au,

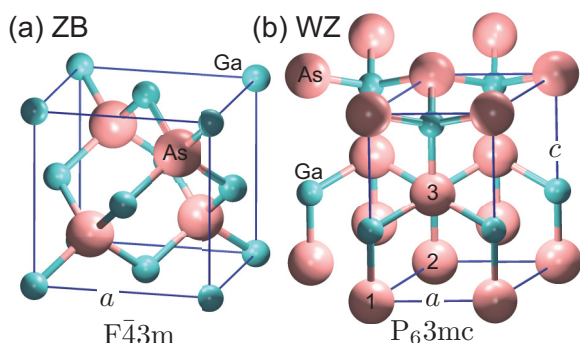


FIG. 1. (Color online) The structures of ZB and WZ GaAs crystals. The conventional unit cells for a ZB and a WZ GaAs crystal are shown in (a) and (b), respectively. The As and Ga atoms are represented by large pink and small green spheres, respectively.

respectively. The generalized-gradient approximation (GGA) is used for the exchange-correlation functional.³⁶ The Brillouin zone integration is performed using the Monkhorst-Pack³⁷ scheme over a $(2 \times 2 \times 2)$ k -point mesh (shifted with respect to the Γ point) for both ZB and WZ supercells. Then the partition length is 0.06 bohr^{-1} or smaller in each direction. Spin-polarized calculations are performed for supercells that contain an odd number of electrons. The optimized kinetic energy cutoff of $E_{\text{cut}} = 250$ eV is used to compute the formation energies of various impurities and defects, whereas an E_{cut} of 200 eV is used for studying V_{As} diffusion in GaAs. The optimized parameters allow us to obtain a relative energy convergence of within 10 meV for all systems presented in this study. The method of a homogeneous background charge is used to model charge states of the defect within the supercell approach. We determined various diffusion paths for V_{As} within the As sublattice of both ZB and WZ GaAs crystals, employing the nudged-elastic-band method.^{38–40} Here, the migration pathway is represented by several intermediate configurations between two fully relaxed end points, and each image is relaxed until the perpendicular forces with respect to the minimum-energy path are less than a given tolerance, which is set to be 0.03 eV/\AA in our calculations.

For ZB GaAs (space group $F\bar{4}3m$), we have obtained the optimized lattice constant of $a = 5.76 \text{ \AA}$, in good agreement with the experimental value of $a = 5.653 \text{ \AA}$.⁴¹ For WZ GaAs (space group P_63mc), we have computed the lattice constants to be $a = 4.05 \text{ \AA}$ and $c = 6.69 \text{ \AA}$. Because bulk WZ GaAs material does not exist, we compare the values only with previous GGA results of $a = 4.050 \text{ \AA}$ and $c = 6.678 \text{ \AA}$.⁴² The calculated direct band gaps of GaAs are 0.17 and 0.22 eV in ZB and WZ crystals, respectively. These results reflect the well-known underestimation of the electronic band gap by semilocal DFT functionals, in particular, when the (too large) theoretical lattice constant is used. In addition, we have performed DFT calculations with the same geometries as in the GGA, but using the hybrid functional proposed by Heyd, Scuseria, and Ernzerhof (HSE).⁴³ Our calculations include 25% of the exact exchange, and the screening parameter is set to be 0.2 \AA^{-1} . The band gaps, which are computed to be 1.15 and 0.99 eV in ZB and WZ GaAs, respectively, are much closer to experimental values. Moreover, we conclude from these calculations that the valence-band maximum experiences a downshift of 0.48 eV in ZB GaAs (0.36 eV in WZ GaAs). These values are in good agreement with recent literature,⁴⁴ and will be used as corrections when our computed results are compared to experiment. The orthorhombic Ga (space group $Cmca$) crystal and trigonal As (space group $R\bar{3}m$) crystal are used to compute the Ga and As chemical potentials.

Since ZB and WZ segments coexist in GaAs nanowires, the band edges from ZB and WZ supercell calculations should be aligned accordingly. We have constructed a 50-atom supercell of a heterostructure of WZ and ZB GaAs. The supercell consists of 13 ZB and 12 WZ bilayers that stack along $[\bar{1}\bar{1}\bar{1}]$ or $[0001]$ for a ZB or a WZ segment, respectively. The constructed heterostructure is optimized for both the lattice constant and the internal coordinates. Note that the lateral dimension of the heterostructure happens to coincide with the average of the WZ and ZB lattice parameters. The valence-band offset

of the ZB and WZ segments can be computed⁴⁵ as

$$\Delta E_{\text{VB}}(\text{GaAs}) = E_v^{\text{ZB}} - E_v^{\text{WZ}} - [E_{\text{core}}^{\text{ZB}}(\text{As}) - E_{\text{core}}^{\text{WZ}}(\text{As})] + [E_{\text{core}}^{\text{ZBseg}}(\text{As}) - E_{\text{core}}^{\text{WZseg}}(\text{As})], \quad (1)$$

where E_v^{ZB} and E_v^{WZ} are the valence-band top energies at the Γ point for ZB and WZ GaAs, respectively, $E_{\text{core}}^{\text{ZB}}(\text{As})$ and $E_{\text{core}}^{\text{WZ}}(\text{As})$ are the core-level energies of As atoms in bulk ZB and WZ GaAs, respectively, and $E_{\text{core}}^{\text{ZBseg}}(\text{As})$ and $E_{\text{core}}^{\text{WZseg}}(\text{As})$ are the core-level energies of As atoms in ZB and WZ segments of the heterostructure, respectively. We compute the band offset to be $\Delta E_{\text{VB}}(\text{GaAs}) = -0.0601$ eV in GGA, in good agreement with the value of -0.0632 eV from a previous calculation.⁴⁶

III. THE ENERGETICS OF DEFECTS AND Au IMPURITIES IN GaAs NANOWIRES

We start by calculating the formation energies of relevant intrinsic defects. The formation energy of a q -charged (q is an integer number) defect (or impurity) X at site Y as a function of the Fermi level ε_F is defined by

$$E_f[X_Y^q, \varepsilon_F] = E[X_Y^q] - E_{\text{host}} - \sum_i n_i \mu_i + q(\varepsilon_F + E_v) + E_{\text{corr}}. \quad (2)$$

Here, $E[X_Y^q]$ is the total energy of a q -charged supercell with a defect X_Y and E_{host} is the energy of a perfect GaAs bulk supercell with the same shape. n_i and μ_i represent the change in the number of species i in the supercell and the chemical potential for a species i , respectively. ε_F is the Fermi level which depends on the doping condition, and E_v is the valence-band top energy of the corresponding bulk GaAs crystal. Due to the $(2 \times 2 \times 2)$ k -point mesh used for supercell calculations, the gap between the highest occupied (HOMO) and the lowest unoccupied (LUMO) molecular orbitals is much higher in these supercell calculations compared to the gap at the Γ point in GaAs bulk calculations. Even though this widened gap is a technical artifact of our method, it puts us in position to vary ε_F in a rather wide range while still maintaining the physically correct charge distribution localized near the defect. The energy interval around E_v in which our calculations can be expected to yield physically meaningful charge transfer levels, as a charged defect cannot transfer charge to the LUMO or from the HOMO, is indicated in the figures. The linear and quadratic correction terms with respect to q of $E_{\text{corr}} = \Delta V q + \alpha q^2 / 2\epsilon L$ account for the spurious electrostatic interaction between periodic images of charged defects.^{47,48} ΔV is a correction for the spurious potential offset induced by the finite defect concentration in the calculation; it is calculated from the energy difference of atomic core levels between a neutral supercell with an X_Y defect and a perfect bulk supercell. The values for α and ϵ , the Madelung constant and the static dielectric constant, respectively, are taken according to the ZB or WZ polytype of bulk GaAs, and L is the supercell dimension used in the corresponding calculations. The values of α , ϵ , and L are listed in Table III in the Appendix for the cases of ZB and WZ GaAs crystals, respectively. Our computed dielectric constant ϵ for ZB GaAs is 32% larger than the experimental value of $0.90 e \text{ \AA}^{-1} \text{ V}^{-1}$.⁴⁹

In the growth conditions, the chemical potentials of Ga and As are in equilibrium with bulk GaAs. Thus, one has the identity $\mu_{\text{Ga}} + \mu_{\text{As}} = \mu_{\text{GaAs}}$, where $\mu_{\text{GaAs}} = -E_{\text{GaAs}}^{\text{bulk}}$ is the cohesive energy per formula unit of the pertinent GaAs polytype. The range of the As chemical potential is specified in accordance with the growth conditions, with the upper bound set to be at the equilibrium with bulk As, i.e., $\mu_{\text{As}}^{\text{upper}} = -E_{\text{As}}^{\text{bulk}}$. The lower bound is set to be at the equilibrium with bulk Ga as $\mu_{\text{As}}^{\text{lower}} = -E_{\text{GaAs}}^{\text{bulk}} + E_{\text{Ga}}^{\text{bulk}}$. Disregarding the difference of the cohesive energies of GaAs of 20 meV in ZB and WZ crystals, we align the upper bound $\mu_{\text{As}}^{\text{upper}}$ for ZB and WZ to the same value. We take the lower bound $\mu_{\text{As}}^{\text{lower}}$ to be 0.7 eV below $\mu_{\text{As}}^{\text{upper}}$, so that $\mu_{\text{As}}^{\text{lower}}$ is very close to a Ga-rich condition for both ZB and WZ GaAs. The bulk energies of GaAs, Ga, and As crystals are calculated using the optimized lattice parameters. Note that the upper and lower bounds of the As chemical potentials correspond to As- and Ga-rich growth conditions, respectively. In addition, the cohesive energy bulk Au per atom is inserted for the Au chemical potential, i.e., $\mu_{\text{Au}} = -E_{\text{Au}}^{\text{bulk}}$.

Figure 2(a) shows the V_{As} formation energies for various charge states q , indicating that the formation energies of V_{As} in WZ are overall lower than those in ZB. The formation energies are computed using Eq. (2), and the potential offsets ΔV associated with the V_{As} defects are listed in Table IV in the Appendix. Under As-rich growth conditions [left y axis in Fig. 2(a)], the formation energies of neutral V_{As} defects are quite high (3.3 and 3.2 eV in ZB and WZ, respectively). Under Ga-rich conditions [right y axis in Fig. 2(a)], the formation energies are lowered by 0.7 eV; however, the energies remain relatively high. Thus, the formation of As vacancies could be energetically unfavorable under the usual GaAs nanowire growth conditions in both ZB and WZ segments. Our results show that V_{As}^+ and V_{As}^- defects are stable at various doping conditions in ZB and WZ GaAs crystals. Deep (+/−) levels are found at $E_v^{\text{ZB}} + 0.44$ and $E_v^{\text{WZ}} + 0.45$ eV in ZB and WZ, respectively. Since GaAs nanowires may have coexisting ZB and WZ segments, it is instructive to specify the charge transfer levels of defects in the WZ segments also with respect to the valence-band edge of the ZB segments, using our results that the valence-band maximum of ZB GaAs is 0.0601 eV lower than in WZ GaAs. Thus, one obtains the (+/−) level in WZ as $E_v^{\text{ZB}} + 0.51$ eV. We found that V_{As}^{2-} and V_{As}^{3-} in both ZB and WZ GaAs crystals are unstable, consistent with Ref. 30, because the structures relax to a GaAs antisite that is neighboring a Ga vacancy. As seen from Fig. 2, the neutral As vacancies are energetically unfavorable, indicating that a V_{As} in GaAs is a so-called “negative- U ” system. Our results are consistent with previous theoretical studies,^{30,50,51} although the quoted absolute positions of the (+/−) levels in these studies are different from ours. For a quantitative comparison, it is important to realize that Schultz and von Lilienfeld³⁰ attempted to set E_v to the true ionization potential, whereas we use the plain DFT GGA value. Estimating the true valence-band top from our HSE calculations, a downshift of 0.4 eV (see Sec. II) should be applied to our E_v value in order to compare to their work, or to experimental data. The same applies when comparing to the values of Komsa and Pasquarello,⁵¹ who performed all their calculations with the HSE functional. With this in mind, our results are in much better agreement with these previous works. It is worth noting that the negative- U

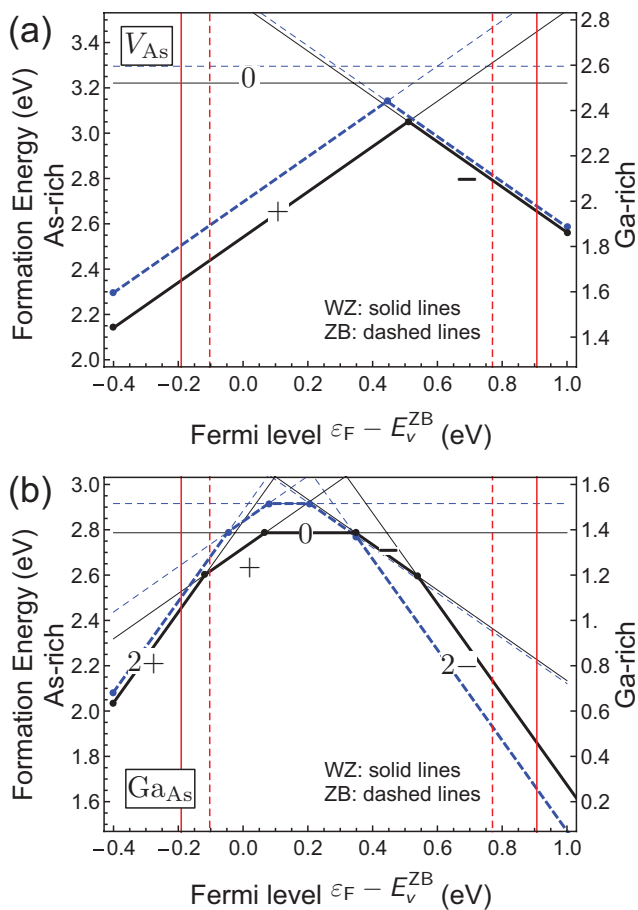


FIG. 2. (Color online) The formation energy of an As vacancy (a) and a Ga antisite (b) in various charge states in GaAs polytypes at different doping conditions, as a function of the Fermi level ϵ_F . The formation energies of As vacancies in ZB GaAs and WZ GaAs are shown as dashed and solid lines, respectively. The thick lines represent stable charge states. The vertical lines indicate the HOMO and LUMO levels in the defect-free supercell and thus delimit the energy interval where the GGA total energies are considered reliable. The left and right y axes show the formation energies under As-rich (μ_{As}^{upper}) and Ga-rich (μ_{As}^{lower}) conditions as described in the text. Here, one has the identity $\mu_{As}^{lower} = \mu_{As}^{upper} - 0.7$ eV.

feature of a V_{As} disappears in their HSE calculations. This is due to the fact that the (negative) contribution of the electronic exchange energy, which is more pronounced in the hybrid functional, energetically favors spin-polarized solutions, e.g., the neutral V_{As} in the present case. Whether this stabilization of a V_{As}^0 in a narrow range of the Fermi level is indeed a physical feature or not should be determined by future experiments.

The Ga antisite Ga_{As} could be another intrinsic defect within a growing GaAs nanowire under As-deficient conditions, and we show the formation energies of Ga_{As} as a function of ϵ_F in Fig. 2(b). The formation energies are computed using Eq. (2), with the potential offset ΔV associated with Ga_{As} defects listed in Table IV in the Appendix. The formation energies are specified for both Ga-rich [right y axis in Fig. 2(b)] and As-rich [left y axis Fig. 2(b)] conditions, and the formation energies are 1.4 eV lower in Ga-rich than in As-rich conditions. In both ZB and WZ GaAs crystals, Ga_{As} defects with charge states from

$2+$ to $2-$ may be stable under certain doping conditions. The associated formation energies in WZ GaAs are overall lower than in ZB GaAs. The Ga_{As}^0 and Ga_{As}^+ defects are energetically more favorable by 0.13–0.14 eV in WZ than in ZB, whereas a Ga_{As}^- defect is only 0.01 eV more stable in WZ. As a result, the charge transfer levels ($0/-$) differ by 0.12 eV in ZB and WZ. It follows that, on an absolute scale, the charge transfer levels are located at $E_v^{ZB} + 0.21$ and 0.33 eV in ZB and WZ segments of a GaAs nanowire, respectively. We notice that both intrinsic defects of V_{As} and Ga_{As} have deep charge transfer levels and they are deeper in WZ GaAs. Comparing Figs. 2(a) and 2(b), one may find that V_{As} are more stable than Ga_{As} defects for the doping conditions of $\epsilon_F - E_v^{ZB} < 0.21$ (0.27) eV in ZB (WZ) under As-rich conditions, while Ga_{As} are more stable than V_{As} defects for the doping conditions of $\epsilon_F - E_v^{ZB} > 0.21$ (0.27) eV in ZB (WZ). When comparing to experiment, one should take into account that the “true” valence-band top is lower than the E_v resulting from our DFT GGA calculations, such that the range of horizontal-axis values plotted in Fig. 2 approximately reflects the “true” band gap.

We also study the energetics of substitutional Au impurities in GaAs crystals, and the computed formation energies of Au_{As} and Au_{Ga} as a function of ϵ_F are shown in Fig. 3. The formation energies of Au_{As} and Au_{Ga} are computed using Eq. (2), with the potential offsets associated with Au_{As} and Au_{Ga} listed in Table IV in the Appendix. Moreover, the formation energies are specified for both Ga-rich (right y axis in Fig. 3) and As-rich (left y axis in Fig. 3) conditions. It is found that under As-rich growth conditions a Au_{Ga} is energetically more favorable than a Au_{As} by about 1–2 eV both in ZB GaAs and in WZ GaAs, depending on the doping conditions. However, under Ga-rich growth conditions, the formation energy of a Au_{Ga} is 0.7 eV higher than that under As-rich conditions, while the formation energy of a Au_{As} becomes 0.7 eV lower. Therefore, under Ga-rich conditions, the Au_{As} defects turn out to be more stable than the Au_{Ga} . We expect that Au_{Ga} defects with charge states from $2+$ to $2-$ may be stable under certain doping conditions. A Au_{Ga} defect has its charge transfer levels mostly in the lower part of the band gap, while the charge transfer levels of a Au_{As} lie at somewhat higher energies. The Au_{As} impurities occur preferentially as $2+$, $+$, or neutral defects, while the levels of negatively charged defects probably already lie above the conduction-band minimum of the host material. Figure 3(a) indicates that the charge transfer levels of Au_{As} defects are deep, $E_v^{ZB} + 0.78$ eV and $E_v^{ZB} + 0.91$ eV for ZB and WZ crystals, respectively. In contrast, a Au_{Ga} impurity switches from a neutral state to a $1-$ charged state at $E_v^{ZB} + 0.22$ eV and $E_v^{ZB} + 0.35$ eV in ZB and WZ crystals, respectively, as seen in Fig. 3(b). As stated before, one should allow for a correction of about 0.4 eV to our E_v value when comparing to experiment. Experimental studies using deep-level transient spectroscopy and photoluminescence spectroscopy^{13–15} have identified a Au-related deep-acceptor level of about 0.4 eV above the valence band in bulk GaAs. Moreover, we find that a Au_{Ga} has a lower formation energy compared to a Au_{As} under the moderately As-rich growth conditions conventionally used. Taking into account the downshift of E_v with respect to the DFT GGA value (see, e.g., Ref. 44), it is plausible that the experimentally observed defect level at 0.4 eV above the valence band is indeed due to Au_{Ga} defects.

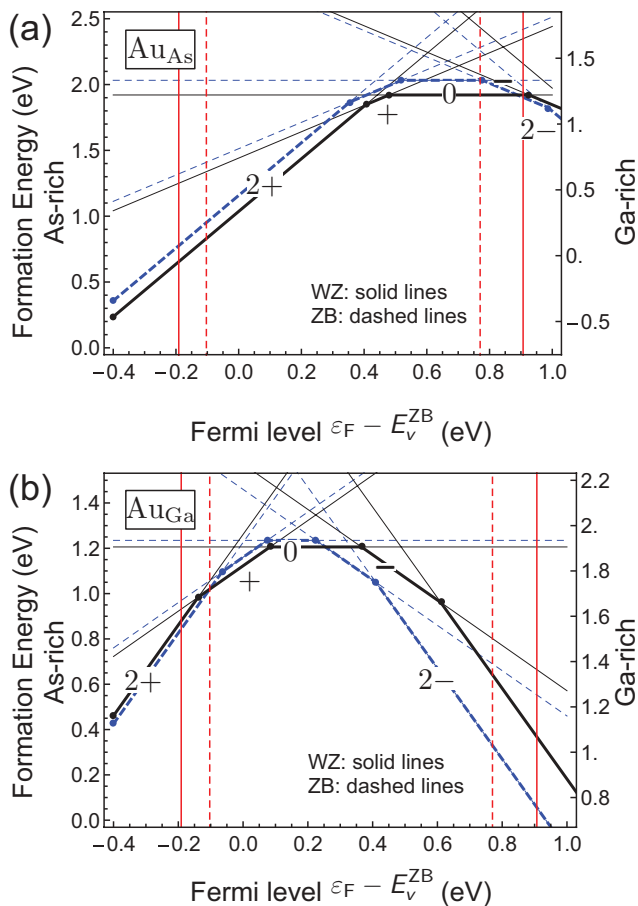


FIG. 3. (Color online) The formation energies of a substitutional Au defect in the ± 1 -charged, ± 2 -charged, and neutral states in WZ and ZB GaAs crystals. The formation energies of a substitutional Au impurity for a lattice As atom and a lattice Ga atom are shown in (a) and (b), respectively. The formation energies of Au impurities in ZB GaAs and WZ GaAs are shown as dashed and solid lines, respectively. The thick lines represent stable charge states. The vertical lines indicate the HOMO and LUMO levels in the defect-free supercell, as in Fig. 2. The left and right y axes show the formation energies under As-rich ($\mu_{\text{As}}^{\text{upper}}$) and Ga-rich ($\mu_{\text{As}}^{\text{lower}}$) conditions as described in the text.

We conclude this section by discussing the energetics of defects caused by a deficiency of arsenic under varying growth conditions. In Fig. 4(a), we compare the formation energies of the lowest-energy V_{As} , Au_{As} , and Ga_{As} defects in p -type ZB and WZ GaAs crystals with the condition $\varepsilon_{\text{F}} - E_{\text{v}}^{\text{ZB}} = 0$, as a function of As chemical potential μ_{As} . Our calculations show that Au_{As} impurities have the lowest formation energies, while V_{As} and Ga_{As} defects have clearly higher formation energies. Figure 4(b) shows the same comparison for n -type ZB and WZ GaAs crystals with $\varepsilon_{\text{F}} = E_{\text{v}}^{\text{ZB}} + 1.0$ eV. Here, a Ga_{As} in the $2-$ charge state has the lowest formation energy, followed by Au_{As} and V_{As} . Consequently, when growing GaAs nanowires with a gold catalyst droplet, some Au_{As} defects will be formed in the GaAs nanowire, in particular for a p -doped material. The Au impurities act as deep centers and are thus detrimental to the optical properties of nanowires. In gold-free self-catalyzed growth, Ga_{As} and V_{As} defects may exist in

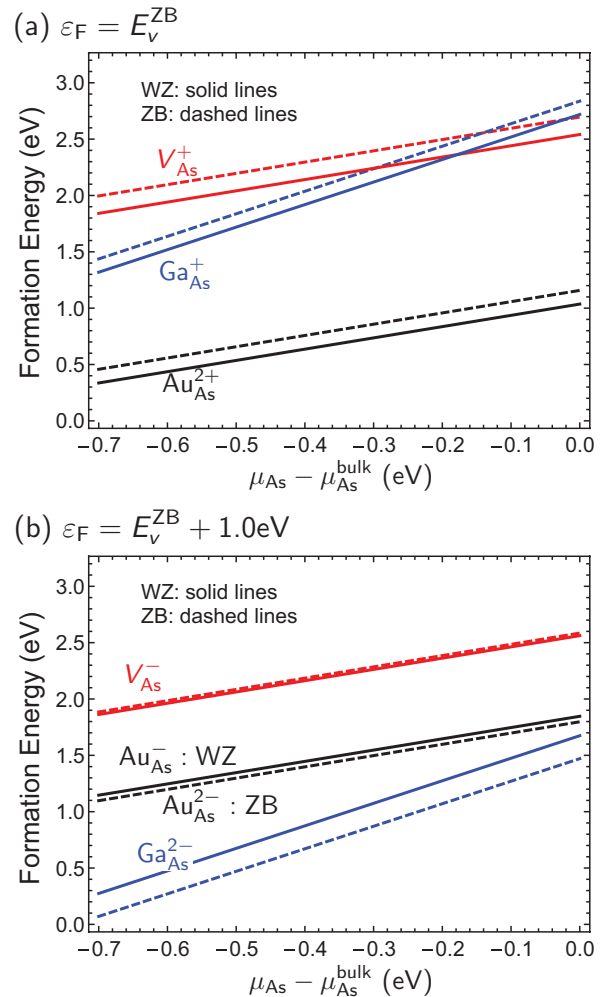


FIG. 4. (Color online) The formation energies of V_{As} , Au_{As} , and Ga_{As} defects in GaAs crystals as a function of μ_{As} . In (a) and (b), the Fermi energy is set to be at the calculated top of the valence band and 1 eV above, respectively, to describe a p -type or an n -type material. Only the energetically most favorable charge states are shown.

the nanowire, albeit at much smaller concentration than the Au defects if the material is p doped. Of these three defect species, only the V_{As} defect is expected to be mobile via a hopping diffusion mechanism. The mobility of the Ga_{As} and Au_{As} defects will most probably be vacancy mediated, and thus require the V_{As} presence. Moreover, it is conceivable that V_{As} hopping diffusion could play a role in the nanowire growth process as a mechanism supplying arsenic to the interfacial growth zone between the nanowire tip and the catalyst droplet. Hence, we will investigate the detailed diffusion processes of V_{As} defects in GaAs crystals in the following section.

IV. As VACANCY DIFFUSION IN GaAs

Arsenic vacancies in GaAs have been characterized experimentally by positron annihilation⁵² and by scanning-tunneling microscopy.⁵³ For ZB GaAs, a number of theoretical studies, using (semi)local DFT (Refs. 30, 54, and 55) or hybrid functionals,^{31,51} have been carried out, and the diffusion pathway of the arsenic vacancy has been investigated.²⁶

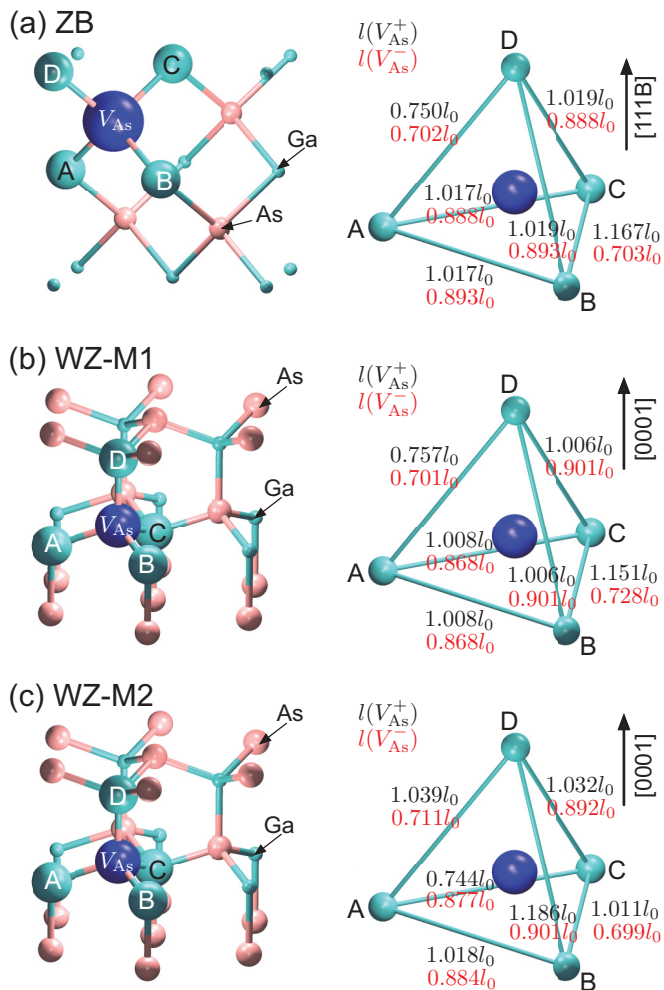


FIG. 5. (Color online) The geometry of V_{As} defects in GaAs crystals. The relaxations of V_{As}^+ and V_{As}^- in ZB GaAs are illustrated in (a), while the relaxations of two sets of stable V_{As}^+ and V_{As}^- in WZ GaAs are characterized in (b) and (c), respectively. We have found two stable V_{As}^+ defects (*M1* and *M2*) and two V_{As}^- (*M1* and *M2*) in WZ GaAs. A V_{As} is highlighted by a big blue sphere, and its four neighboring Ga atoms are highlighted by spheres labeled A, B, C, and D. These neighboring Ga atoms form a tetrahedron. The other attached As and Ga atoms are represented by small pink and large green spheres, respectively. The right panel indicates the relaxed edge length of the Ga tetrahedron. The upper and lower numbers refer to a V_{As}^+ and a V_{As}^- , respectively.

Interestingly, these calculations claimed the existence of a metastable interstitial state along the diffusion path in ZB GaAs, while this issue is unexplored for WZ GaAs.

We start by characterizing the geometry of V_{As} defects in GaAs crystals in more detail. As shown in Fig. 5, the neighboring Ga atoms with respect to a V_{As} define a Ga tetrahedron. To specify the local deformation of a crystal due to the V_{As} presence, we study the relaxation of the edge length l of the tetrahedron and compare it to the equilibrium distance between two neighboring Ga atoms in the ZB (WZ) GaAs crystal of $l_0 = 4.07$ (4.05) Å. Similarly, the relaxed tetrahedron volume V will be compared to the equilibrium tetrahedron volume in ZB (WZ) GaAs crystal of $V_0 = 7.97$ (7.93) Å³.

TABLE I. Ga tetrahedron volumes of V_{As} in various charge states. V_0 represents the equilibrium tetrahedron volume in a ZB (WZ) GaAs crystal of $V_0 = 7.97$ (7.93) Å³.

	V_{As}^+	V_{As}^0	V_{As}^-
ZB	0.922 V_0	0.757 V_0	0.516 V_0
WZ <i>M1</i>	0.896 V_0	0.696 V_0	0.518 V_0
WZ <i>M2</i>	0.926 V_0		0.512 V_0

For a V_{As}^- in ZB GaAs, the edge lengths of the Ga-atom tetrahedron are all contracted [see the right panel of Fig. 5(a)], resulting in a significantly reduced volume of $V = 0.516V_0$ (48.4% compression) as listed in Table I. In particular, the A-D and B-C edges are most contracted by up to $l = 0.702l_0$ (29.8% compression), while other edges are compressed by $\sim 11\%$. The deformation reduces the symmetry of the distorted Ga tetrahedron to D_{2d} which is in accordance with previous studies.^{54,55} In WZ GaAs, there exist two different, but energetically very similar structures (*M1* and *M2*) for a relaxed V_{As}^- [see Figs. 5(b) and 5(c)]. The WZ *M2* configuration is slightly more stable than the WZ *M1* configuration in terms of energetics. Both WZ *M1* and WZ *M2* V_{As}^- configurations exhibit similar deformations as a V_{As}^- in ZB, and the relaxed tetrahedron volumes are reduced by 48.4% to 48.8%, respectively. This is comparable to the ZB case. The relaxed Ga tetrahedron for WZ *M1* and WZ *M2* V_{As}^- defects possesses a C_{2v} and a C_1 symmetry, respectively.

For a V_{As}^+ , the tetrahedron of neighboring Ga atoms contracts in volume by only 7.8% in ZB GaAs, whereas it contracts by 7.4% to 11.4% in WZ GaAs, as listed in Table I. In particular, V_{As}^+ defects have one edge compressed, while the other edges are slightly expanded. The WZ *M2* V_{As}^+ configuration has the A-C edge (within the *ab* plane) compressed. In contrast, the WZ *M1* V_{As}^+ configuration has the A-D edge (out of the *ab* plane) compressed. In other words, the deformation of V_{As}^+ in WZ GaAs is anisotropic, and hence the relaxed Ga tetrahedron for WZ *M1* and WZ *M2* V_{As}^+ defects possesses C_{2v} or C_1 symmetry, respectively. In addition, despite the neutral state being unstable, we mention that the volumes of neutral As vacancies are 0.757 V_0 in ZB and 0.696 V_0 in WZ *M1*, respectively. It is worth noting that the vacancy volume becomes smaller with increasing electronic charge. The physical reason for this general trend lies in the fact that the additional electrons in the vacancy allow for the filling of orbitals with bonding character that are formed by symmetry-adapted linear combinations of the Ga dangling-bond orbitals.

In the following, we assume that the V_{As} diffusion proceeds via a neighboring As atom of the arsenic sublattice hopping into the vacancy. Schematically, an As atom hops out of an initial Ga-tetrahedron cage into an adjacent target Ga-tetrahedron cage that previously enclosed the As vacancy site. We refer to the tetrahedron that surrounds the migrating As atom as the initial tetrahedron, and refer to the adjacent Ga tetrahedron that surrounds the target As vacancy site as the target tetrahedron. We note that the reverse process occurs with the same probability, with the roles of initial and target tetrahedrons interchanged. The diffusion process can be decomposed into an As escape from the initial tetrahedron, its

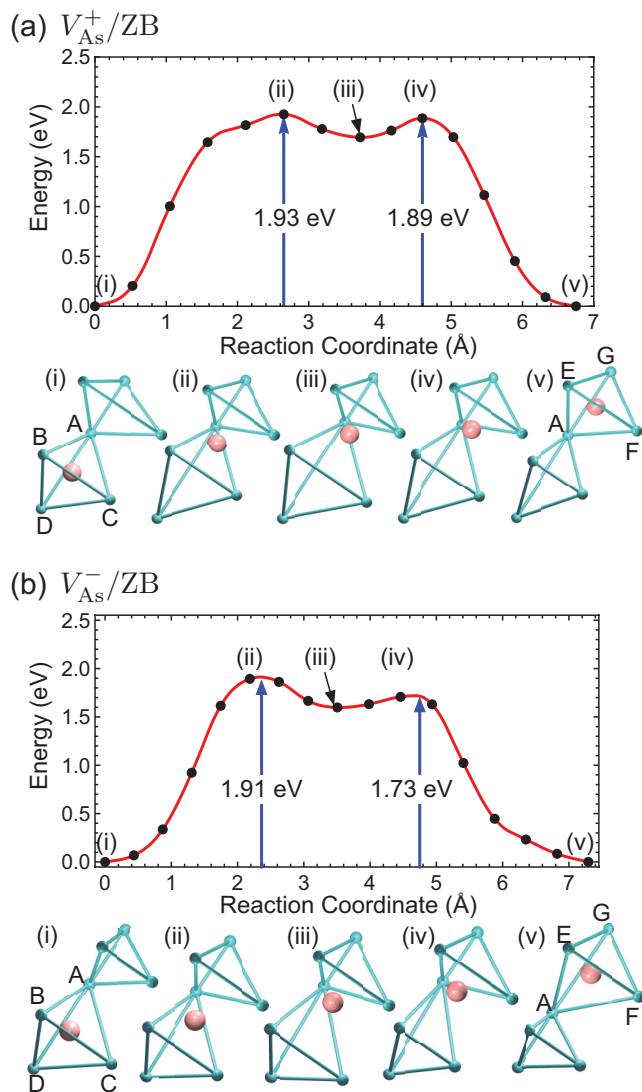


FIG. 6. (Color online) The energy paths of V_{As}^{1+} (a) and V_{As}^{1-} (b) diffusion in ZB GaAs. The structures of two ground-state minima [(i) and (v)], an interstitial state (iii), and transition states [(ii) and (iv)] are illustrated. The As and Ga atoms are represented by larger pink and smaller green spheres, respectively.

interstitial motion between the two tetrahedra, and an entry into the target tetrahedron. Note that one of the Ga atoms is located at the common apex of both tetrahedra.

Since ZB GaAs is a cubic crystal, the four possible diffusion paths of a V_{As} to four neighboring As sites are symmetrically equivalent. The diffusion path shown Fig. 6 is sufficient to describe As diffusion in ZB GaAs. Figure 6(a) illustrates the detailed diffusion process of a V_{As}^{1+} in ZB GaAs, indicating an overall migration barrier of 1.93 eV. The local minimum configurations [(i) and (v) in Fig. 6(a)] as well as the saddle point configurations [(ii) and (iv) in Fig. 6(a)] along the diffusion path are illustrated by the ball-and-stick models in the figure. In the target tetrahedron, the A - G edge corresponds to the short edge [A - D in Fig. 5(a)]. By expanding the bond between As and Ga at the D site, the diffusing As atom escapes from the initial tetrahedron. During the escape process, the initial tetrahedron is expanding, while the target

tetrahedron is contracting. After passing through the ABC face of the tetrahedron, the diffusing As atom arrives at the first saddle point (ii) which represents the transition state for V_{As}^{1+} migration. In this configuration, the As-Ga bonds to the initial tetrahedron apexes are broken except for the A -site. The target tetrahedron volume is compressed from $0.922V_0$ to $0.719V_0$ which corresponds to the volume of a neutral As vacancy (see Table I). This observation implies that a positively charged As vacancy in the target tetrahedron attracts electrons ahead of the As migration. When migrating toward the target tetrahedron in the interstitial space, the diffusing As atom reaches an interstitial state (iii) with a shallow energy dip. At this moment, the diffusing As atom is located at an octahedral interstitial site in ZB GaAs. In this interstitial state, the migrating As creates two additional bonds to target tetrahedron apexes, indicating that the As atom starts to supply electrons to the target tetrahedron. Consequently, the target tetrahedron volume further contracts to $0.662V_0$. This volume is still a bit larger than for a negatively charged As vacancy, but notably smaller than for a neutral As vacancy. Passing through the AEF face of the target tetrahedron, the diffusing As atom enters the target vacancy. The diffusion process is thus completed. When the As atom diffuses into the target tetrahedron, it establishes the As-Ga bond to the G site. The migration from the octahedral interstitial site to the final state has a shallow migration barrier of 0.19 eV, which is 0.04 eV lower than the backward diffusion barrier. We note that the contraction of the A - G edge of the empty target tetrahedron has moved over to the B - C edge of the (finally empty) initial tetrahedron.

Figure 6(b) shows the V_{As}^{1-} diffusion path in ZB GaAs, which is similar to V_{As}^{1+} diffusion with a slightly lower migration barrier of 1.91 eV. Again, we find the escape barrier from the initial tetrahedron to be the rate-limiting step. In the interstitial space, there is also an interstitial As configuration located in a shallow dip, and it occupies an octahedral interstitial site in ZB GaAs. The associated initial and target tetrahedra at this stage have volumes of $1.102V_0$ and $0.673V_0$, respectively. We note that the tetrahedron volume expands while losing an electron (see Table I). The diffusing As atom at the interstitial site has to overcome an entry barrier of 0.13 eV to migrate into the target tetrahedron, which is 0.19 eV lower than that of the reverse diffusion process. The initial tetrahedron volume is reduced to the V_{As}^{1-} value after the diffusing As passes through the second saddle point. We note that the two saddle points along the diffusion path have different energies. Although an oversimplified consideration solely based on the atomic positions suggests that a symmetric mechanism might exist, the observed symmetry breaking is physical because the charge balance between the two tetrahedra under the presence of the migrating As atom is nonsymmetric. Therefore, it is meaningful to distinguish between whether the escape (first) saddle point or the entry (second) saddle point is rate limiting.

Our results qualitatively agree with a previous theoretical study,²⁶ which reported migration barriers of 2.41 and 2.38 eV for V_{As}^{1+} and V_{As}^{1-} diffusion in ZB GaAs, respectively, using atomic-orbital basis sets. Both in their and in our work, the computed diffusion barrier of a V_{As}^{1-} is slightly lower than that of a V_{As}^{1+} . However, in our plane-wave-based calculations, the diffusion barriers of V_{As}^{1+} and V_{As}^{1-} are computed to be 1.93

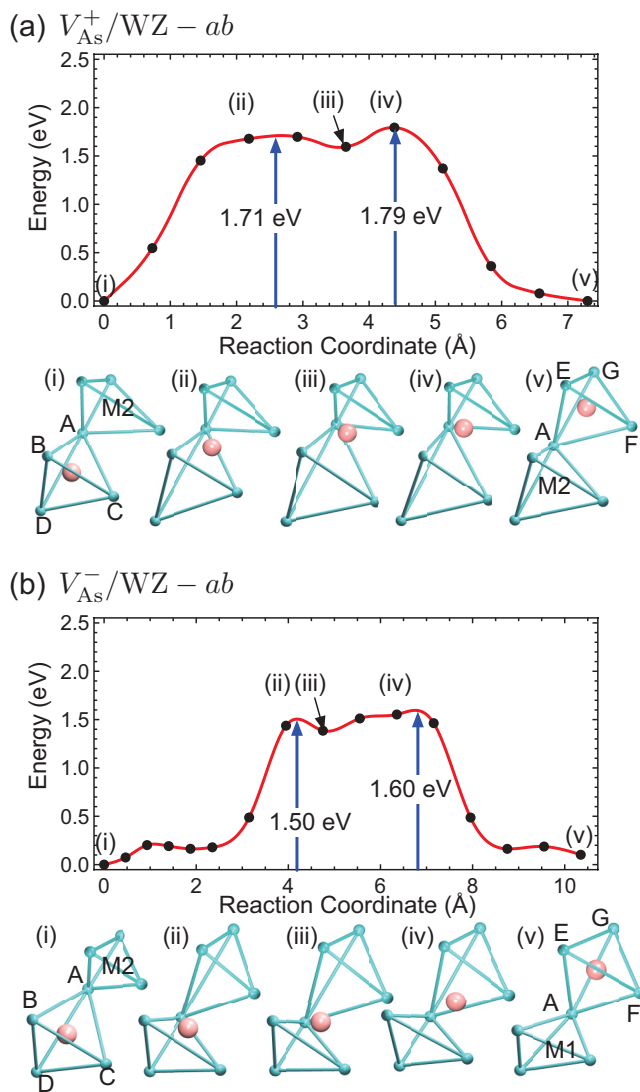


FIG. 7. (Color online) The energy paths of V_{As}^{1+} (a) and V_{As}^{1-} (b) diffusion in the ab plane of WZ GaAs. The structures of two ground-state minima [(i) and (v)], an interstitial state (iii), and transition states [(ii) and (iv)] are illustrated. The color scheme is the same as in Fig. 6.

and 1.91 eV, respectively, which are about 0.5 eV lower in energy than the values reported in Ref. 26. We believe that these differences are due to the more complete basis set for the wave functions in our calculations, which allows for a more accurate description of the energetics, in particular in transition-state geometries.

Next, we perform analogous calculations for V_{As}^{+} and V_{As}^{-} diffusion in WZ GaAs. Due to the lower crystal symmetry of WZ, one needs to consider two pathways; i.e., an As vacancy can diffuse within the ab plane by hopping from site 1 to site 2 or along the c axis by hopping from site 2 to site 3, as illustrated in Fig. 1(b). First, we discuss the vacancy diffusion within the ab plane. Figure 7 shows that V_{As}^{+} and V_{As}^{-} can diffuse in the ab plane in WZ GaAs with migration barriers of 1.79 and 1.60 eV, respectively. As discussed above, there are two different minimum configurations for V_{As}^{+} and V_{As}^{-} defects, $M1$ and $M2$, in WZ GaAs. The transition from the

more stable $M2$ to the $M1$ configuration costs relatively low activation energies, 0.11 eV for a V_{As}^{+} and 0.17 eV for a V_{As}^{-} . We basically find similar diffusion processes as in ZB GaAs, i.e., an As escape from the initial tetrahedron, an As motion within the interstitial space, and an As entry into the target tetrahedron. In the intermediate configuration in the ab plane, the As atom is located in an octahedral interstitial site in WZ GaAs. Thus, the local symmetry of the intermediate is the same for WZ and ZB along this path. However, the overall migration barriers are up to 0.2–0.3 eV lower in WZ than in ZB. In the V_{As}^{-} diffusion, we note that the volume contraction of the initial tetrahedron takes place earlier than in the other cases [see Fig. 7(b)], i.e., its volume is reduced to $0.691V_0$ when As reaches the interstitial configuration. In comparison, for V_{As}^{-} diffusion in ZB GaAs, the initial tetrahedron has a volume of $1.102V_0$ when the diffusing As is at the interstitial site. Moreover, for V_{As}^{+} defects in WZ and ZB crystals, the associated initial tetrahedron volume is about $1.8V_0$ to $1.9V_0$ when the diffusing As is at the interstitial site. This early compression of the initial tetrahedron for the V_{As}^{-} diffusion also results in a compressed interstitial space. In the interstitial space, the diffusing As atom forms three bonds to the target tetrahedron and one bond to the initial tetrahedron. Hence, the interstitial V_{As}^{-} is fully coordinated. This could explain the low migration barrier of 1.60 eV associated with the V_{As}^{-} diffusion within the ab plane in WZ GaAs.

Second, we discuss the V_{As} diffusion along the c axis in WZ GaAs. Figure 8 shows that V_{As}^{+} and V_{As}^{-} defects can diffuse along the c axis with relatively high migration barriers of 2.44 and 2.07 eV, respectively. Again, the diffusion process consists of the three steps introduced above: The diffusing As atom escapes from the initial tetrahedron cage through the ABC face. It enters the neighboring octahedral interstitial area through the ABF face and finally hops into the target tetrahedron through the AFG face. When the diffusing As passes the ABF face, it almost crosses the $A-F$ edge. This may result in the high migration barriers associated with the c -axis diffusion in WZ GaAs. For the V_{As}^{-} diffusion, there exists a stable interstitial configuration (iii) as shown in Fig. 8(b). For this configuration, the diffusing As atom is located at a tetrahedral interstitial site. It is fully coordinated and its energy is only 1.03 eV above the ground-state (i) configuration. This may result in the lower V_{As}^{-} migration barrier of 2.07 eV compared to the V_{As}^{+} diffusion as shown in Fig. 8.

Finally, we discuss the possibility of reducing the concentration of V_{As} defects in nanowires by annealing under an arsenic atmosphere. We use the migration barrier of 1.93 eV of a V_{As}^{+} in ZB GaAs to estimate the required annealing time. The diffusivity associated with the V_{As} can be estimated as

$$D \approx a_0^2 \nu_0 \exp(-\Delta E/k_B T), \quad (3)$$

where $\nu_0 = 10^{13}/\text{s}$ is the estimated attempt frequency, k_B is the Boltzmann constant, the annealing temperature is set to be $T = 700$ K, ΔE is the migration energy of an arsenic vacancy in GaAs, and a_0 is the distance between two neighboring As atoms in a GaAs crystal and is also the hop distance for V_{As} diffusion. In a nanowire growing along the $[\bar{1}\bar{1}\bar{1}]$ direction, V_{As} defects are expected to diffuse to the sidewall. Using a typical radius of a GaAs nanowire, $R = 20$ nm (Ref. 7), the annealing time required to remove the V_{As} defects can be computed as

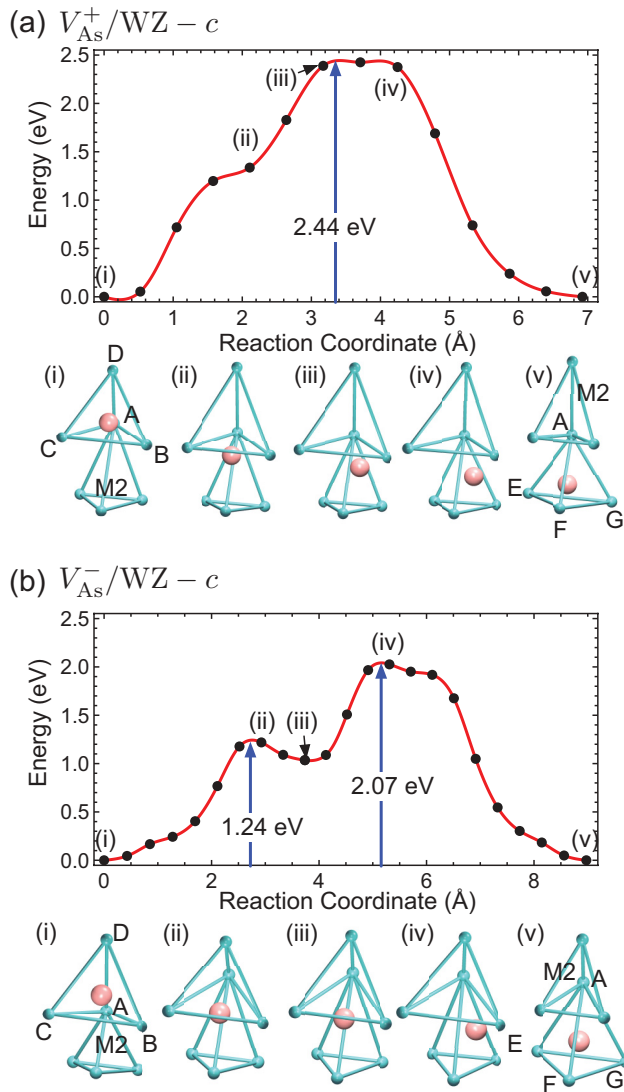


FIG. 8. (Color online) The energy paths of V_{As}^+ (a) and V_{As}^- (b) diffusion along the c axis in WZ GaAs. The structures of various stages (i)–(v) are illustrated. The color scheme is the same as in Fig. 6.

$t = R^2/D = 5.26$ h. In WZ GaAs, the reduction of the energy barrier by 0.14 eV to 1.79 eV reduces the annealing time by a factor of 10 to 31.3 min. Thus, we conclude that the V_{As} defects introduced in a GaAs nanowire during As-deficient growth can be annealed within a reasonable time frame at a temperature of 700 K. We hereby summarize the diffusivities of V_{As}^+ and V_{As}^- defects in ZB and WZ GaAs crystals for various diffusion processes in Table II.

TABLE II. Diffusion constants for V_{As} diffusion in ZB and WZ GaAs at $T = 700$ K. All numbers are given in units of cm^2/s . The V_{As} diffusivity along the c direction in WZ GaAs is the lowest.

	ZB	WZ ab	WZ c
V_{As}^+	2.11×10^{-16}	2.13×10^{-15}	4.46×10^{-20}
V_{As}^-	2.94×10^{-16}	4.97×10^{-14}	2.05×10^{-17}

V. DISCUSSION AND SUMMARY

Using DFT calculations, we have characterized the V_{As} , Ga_{As} , and Au defects in GaAs crystals that may be introduced in GaAs nanowires grown with the help of metal droplets under As-deficient conditions at the interfacial growth zone. The substitutional Ga_{As} , Au_{As} , and Au_{Ga} defects exhibit similar formation energies and defect levels in both ZB and WZ GaAs crystals. Moreover, a V_{As} defect behaves as a negative- U system, switching from a V_{As}^+ in a p -doped material to a V_{As}^- in an n -doped material, for both GaAs crystals. If a Au droplet is used a catalyst for nanowire growth, the formation of substitutional Au impurities is possible and is found to be energetically more favorable than the formation of Ga_{As} or V_{As} defects. Moreover, we have shown that it is energetically more favorable by about 1 to 2 eV for a Au substitutional impurity to replace a lattice Ga atom than a lattice As atom in either ZB or WZ GaAs. Given that DFT GGA calculations give a too small band gap, the calculated acceptor level of Au_{Ga} at $E_v + 0.22$ eV is found to be in reasonable agreement with the experimental value of $E_v + 0.4$ eV in ZB GaAs.

In Au-free, self-catalyzed growth of nanowires that are grown at higher temperatures,⁵⁶ the formation of Ga_{As} could be expected. In particular, for Ga-rich growth conditions and n -type material, the $\text{Ga}_{\text{As}}^{2-}$ species has a low formation energy. This could lead to growth of nonstoichiometric Ga-enriched GaAs.^{7,11} The incorporation of $\text{Ga}_{\text{As}}^{2-}$ will counteract the n -type doping by deliberately added donor species. This may explain why it is rather difficult to obtain n -type conductivity in ZB GaAs nanowires, and only high concentrations of Sn_{Ga} have proven successful so far.⁵⁷ Under less Ga-rich growth conditions, the formation of V_{As} defects could be expected, and their diffusion might even play a role in material transport in the growth of a GaAs nanowire. We note that As interstitials, which could in principle also contribute to As mass transport, tend to have a higher formation energy than V_{As} , except in very As-rich conditions.³⁰ Since we are interested in the As-deficient growth conditions below the nanoparticle, we do not consider As interstitial diffusion here. Our results show that (i) V_{As} defects can diffuse within ZB GaAs with a migration barrier of about 1.9 eV; and (ii) V_{As} defects diffuse favorably within the ab plane in WZ GaAs with somewhat lower migration barriers of 1.6 to 1.8 eV. Based on these results, we estimate that it takes about 5 h to anneal the V_{As} defects at 700 K in a ZB GaAs nanowire, but only 30 min in a WZ nanowire. Thus, annealing of GaAs nanowires under an arsenic atmosphere could be useful in obtaining samples with a longer lifetime for the charge carriers. However, the diffusivity of V_{As} in the nanowires is too low to contribute substantially to the arsenic supply in the nanowire growth zone, in particular in WZ GaAs, where the diffusion barrier along the c axis is higher than in ZB GaAs.

ACKNOWLEDGMENTS

We acknowledge the Center for Computational Sciences and Simulation (CCSS) of University Duisburg-Essen for computer time and the Deutsche Forschungsgemeinschaft DFG for financial support through Project No. KR 2057/5-1.

TABLE III. The Madelung constants (α), the dielectric constants (ϵ), and the dimension of GaAs supercells (L) for computing the formation energy as described in Eq. (2). The values are listed for both ZB and WZ GaAs supercells. For convenience, ϵ is given in units of $e \text{ \AA}^{-1} \text{ V}^{-1}$. The dimensionless dielectric constant is obtained by multiplying this value by 14.4.

	α	ϵ	L (Å)
ZB	1.638	1.18	17.29
WZ	1.641	1.12	12.16

APPENDIX: PARAMETERS FOR COMPUTING FORMATION ENERGIES

The Madelung constants, the calculated dielectric constants, and the dimensions of ZB and WZ GaAs crystals are listed in Table III. L represents the distance between

TABLE IV. The values of the potential offset corrections for V_{As} ($\Delta V_{V@As}$), Au_{As} ($\Delta V_{\text{Au}@As}$), Au_{Ga} ($\Delta V_{\text{Au}@Ga}$), and Ga_{As} ($\Delta V_{\text{Ga}@As}$) defects in WZ and ZB GaAs crystals. All numbers are given in units of eV.

	$\Delta V_{V@As}$	$\Delta V_{\text{Au}@As}$	$\Delta V_{\text{Au}@Ga}$	$\Delta V_{\text{Ga}@As}$
ZB	-0.05	-0.01	-0.04	-0.05
WZ	-0.09	-0.02	-0.02	-0.09

the nearest-neighbor defects within a supercell. It is taken to be length of the a axis of a 216-atom ZB and a 96-atom WZ GaAs crystal as listed in Table III. The dielectric constants are the ϵ_{aa} components of the pertinent dielectric tensors. They include both electronic and ionic contributions. The values of the potential offset corrections for various defect and impurity calculations are listed in Table IV.

*yaojun.du@uni-due.de

¹L. Samuelson, *Mater. Today* **6**(10), 22 (2003).

²A. R. Guichard, D. N. Barsic, S. Sharma, T. I. Kamins, and M. L. Brongersma, *Nano Lett.* **6**, 2140 (2006).

³J. R. Maiolo III, B. M. Kayes, M. A. Filler, M. C. Putnam, M. D. Kelzenberg, H. A. Atwater, and N. S. Lewis, *J. Am. Chem. Soc.* **129**, 12346 (2007).

⁴Y. Cui and C. M. Lieber, *Science* **291**, 851 (2001).

⁵C. Thelander, P. Agarwal, S. Brongersma, J. Eymery, L. F. Feiner, A. Forchel, M. Scheffler, W. Riess, B. J. Ohlsson, U. Gösele *et al.*, *Mater. Today* **9**(10), 28 (2006).

⁶L. Jensen, M. Björk, S. Jeppesen, A. Persson, B. Ohlsson, and L. Samuelson, *Nano Lett.* **4**, 1961 (2004).

⁷A. I. Persson, M. W. Larsson, S. Stenström, B. J. Ohlsson, L. Samuelson, and L. R. Wallenberg, *Nat. Mater.* **3**, 677 (2004).

⁸J. C. Harmand, G. Patriarche, N. Péré-Laperne, M.-N. Mérat-Combes, L. Travers, and F. Glas, *Appl. Phys. Lett.* **87**, 203101 (2005).

⁹K. A. Dick, K. Deppert, L. S. Karlsson, L. R. Wallenberg, L. Samuelson, and W. Seifert, *Adv. Funct. Mater.* **15**, 1603 (2005).

¹⁰K. Dick, K. Deppert, T. Martensson, B. Mandl, L. Samuelson, and W. Seifert, *Nano Lett.* **5**, 761 (2005).

¹¹M. J. Tambe, S. Ren, and S. Gradečak, *Nano Lett.* **10**, 4584 (2010).

¹²S. Breuer, C. Pfüller, T. Flissikowski, O. Brandt, H. T. Grahn, L. Geelhaar, and H. Riechert, *Nano Lett.* **11**, 1276 (2011).

¹³P. Hiesinger, *Phys. Status Solidi A* **33**, K39 (1976).

¹⁴Z. X. Yan and A. G. Milnes, *J. Electrochem. Soc.* **129**, 1353 (1982).

¹⁵V. Pandian, Y. N. Mohapatra, and V. Kumar, *Jpn. J. Appl. Phys.* **30**, 2815 (1991).

¹⁶F. Jabeen, G. Bulgarini, N. Akopian, G. Patriarche, V. Zwiller, and J.-C. Harmand, in *Proceedings of NWG-06*, edited by V. G. Dubrovskii (Publishing Department of St. Petersburg Academic University, St. Petersburg, 2012).

¹⁷M. Bar-Sadan, J. Barthel, H. Shtrikman, and L. Houben, *Nano Lett.* **12**, 2352 (2012).

¹⁸J. Dabrowski and M. Scheffler, *Phys. Rev. B* **40**, 10391 (1989).

¹⁹D. T. J. Hurle, *J. Appl. Phys.* **107**, 121301 (2010).

²⁰K. Haraguchi, K. Hiruma, K. Hosomi, M. Shirai, and T. Katsuyama, *J. Vac. Sci. Technol. B* **15**, 1685 (1997).

²¹V. G. Dubrovskii, G. E. Cirlin, I. P. Soshnikov, A. A. Tonkikh, N. V. Sibirev, Y. B. Samsonenko, and V. M. Ustinov, *Phys. Rev. B* **71**, 205325 (2005).

²²V. Pankoke, S. Sakong, and P. Kratzer, *Phys. Rev. B* **86**, 085425 (2012).

²³P. Kratzer, S. Sakong, and V. Pankoke, *Nano Lett.* **12**, 943 (2012).

²⁴P. Hohenberg and W. Kohn, *Phys. Rev.* **136**, B864 (1964).

²⁵W. Kohn and L. J. Sham, *Phys. Rev.* **140**, A1133 (1965).

²⁶F. El-Mellouhi and N. Mousseau, *Appl. Phys. A* **86**, 309 (2007).

²⁷I. P. Soshnikov, G. É. Cirlin, A. A. Tonkikh, Y. B. Samsonenko, V. G. Dubrovskii, V. M. Ustinov, O. M. Gorbenko, D. Litvinov, and D. Gerthsen, *Phys. Solid State* **47**, 2213 (2005).

²⁸D. Spirkoska, J. Arbiol, A. Gustafsson, S. Conesa-Boj, F. Glas, I. Zardo, M. Heigoldt, M. H. Gass, A. L. Bleloch, S. Estrade *et al.*, *Phys. Rev. B* **80**, 245325 (2009).

²⁹U. Jahn, J. Lähnemann, C. Pfüller, O. Brandt, S. Breuer, B. Jenichen, M. Ramsteiner, L. Geelhaar, and H. Riechert, *Phys. Rev. B* **85**, 045323 (2012).

³⁰P. A. Schultz and O. A. von Lilienfeld, *Modell. Simul. Mater. Sci. Eng.* **17**, 084007 (2009).

³¹H.-P. Komsa and A. Pasquarello, *Physica B* **407**, 2833 (2012).

³²P. E. Blöchl, *Phys. Rev. B* **50**, 17953 (1994).

³³G. Kresse and D. Joubert, *Phys. Rev. B* **59**, 1758 (1999).

³⁴G. Kresse and J. Hafner, *Phys. Rev. B* **47**, 558(R) (1993).

³⁵G. Kresse and J. Furthmüller, *Phys. Rev. B* **54**, 11169 (1996).

³⁶J. P. Perdew, K. Burke, and M. Ernzerhof, *Phys. Rev. Lett.* **77**, 3865 (1996); **78**, 1396(E) (1997).

³⁷H. J. Monkhorst and J. D. Pack, *Phys. Rev. B* **13**, 5188 (1976).

³⁸H. Jónsson, G. Mills, and K. W. Jacobsen, in *Classical and Quantum Dynamics in Condensed Phase Simulations*, edited by B. J. Berne, G. Ciccotti, and D. F. Coker (World Scientific, Singapore, 1998), pp. 385–404.

³⁹G. Henkelman, B. P. Uberuaga, and H. Jónsson, *J. Chem. Phys.* **113**, 9901 (2000).

⁴⁰G. Henkelman and H. Jónsson, *J. Chem. Phys.* **113**, 9978 (2000).

- ⁴¹*Semiconductors, Group IV Elements and III-V Compounds*, edited by O. Madelung, Landolt-Börnstein Database, Group III, Vol. 41A1a (Springer-Verlag, Berlin, 1991).
- ⁴²T. Cheiwchanamngij and W. R. L. Lambrecht, *Phys. Rev. B* **84**, 035203 (2011).
- ⁴³J. Heyd, G. E. Scuseria, and M. Ernzerhof, *J. Chem. Phys.* **118**, 8207 (2003).
- ⁴⁴W. Chen and A. Pasquarello, *Phys. Rev. B* **86**, 035134 (2012).
- ⁴⁵A. Franciosi and C. G. V. de Walle, *Surf. Sci. Rep.* **25**, 1 (1996).
- ⁴⁶A. De and C. E. Pryor, *Phys. Rev. B* **81**, 155210 (2010).
- ⁴⁷C. G. Van de Walle and J. Neugebauer, *J. Appl. Phys.* **95**, 3851 (2004).
- ⁴⁸G. Makov and M. C. Payne, *Phys. Rev. B* **51**, 4014 (1995).
- ⁴⁹W. J. Moore and R. T. Holm, *J. Appl. Phys.* **80**, 6939 (1996).
- ⁵⁰F. El-Mellouhi and N. Mousseau, *Phys. Rev. B* **71**, 125207 (2005).
- ⁵¹H.-P. Komsa and A. Pasquarello, *J. Phys.: Condens. Matter* **24**, 045801 (2012).
- ⁵²K. Saarinen, P. Hautojärvi, P. Lanki, and C. Corbel, *Phys. Rev. B* **44**, 10585 (1991).
- ⁵³J. Gebauer, R. Krause-Rehberg, C. Domke, P. Ebert, K. Urban, and T. E. M. Staab, *Phys. Rev. B* **63**, 045203 (2001).
- ⁵⁴K. Laasonen, R. M. Nieminen, and M. J. Puska, *Phys. Rev. B* **45**, 4122 (1992).
- ⁵⁵L. Gilgien, G. Galli, F. Gygi, and R. Car, *Phys. Rev. Lett.* **72**, 3214 (1994).
- ⁵⁶F. Jabeen, V. Grillo, S. Rubini, and F. Martelli, *Nanotechnology* **19**, 275711 (2008).
- ⁵⁷C. Gutsche, A. Lysov, I. Regolin, K. Blekker, W. Prost, and F.-J. Tegude, *Nanoscale Res. Lett.* **6**, 65 (2011).